

Lightweight Dynamic Modeling of Cable-Driven Continuum Robots Based on Actuation-Space Energy Formulation

Fangju Yang¹, Hang Yang¹, Ibrahim Alsarraj¹, Yuhao Wang¹, Ke Wu¹

Abstract—Cable-driven continuum robots (CDCRs) require accurate, real-time dynamic models for high-speed dynamics prediction or model-based control, making such capability an urgent need. In this paper, we propose the Lightweight Actuation-Space Energy Modeling (LASEM) framework for CDCRs, which formulates actuation potential energy directly in actuation space to enable lightweight yet accurate dynamic modeling. Through a unified variational derivation, the governing dynamics reduce to a single partial differential equation (PDE), requiring only the Euler moment balance while implicitly incorporating the Newton force balance. By also avoiding explicit computation of cable–backbone contact forces, the formulation simplifies the model structure and improves computational efficiency while preserving geometric accuracy and physical consistency. Importantly, the proposed framework for dynamic modeling natively supports both force-input and displacement-input actuation modes, a capability seldom achieved in existing dynamic formulations. Leveraging this lightweight structure, a Galerkin space–time modal discretization with analytical time-domain derivatives of the reduced state further enables an average 62.3% computational speedup over state-of-the-art real-time dynamic modeling approaches.

Index terms—Cable-driven continuum robot; Lightweight dynamic modeling; Actuation-space energy formulation; Functional variation.

I. INTRODUCTION

Cable-driven continuum robots (CDCRs) require accurate, real-time dynamic models to support high-speed motion prediction and model-based control, especially in fast manipulation and dynamic interaction scenarios [1]. Representative scenarios include oscillatory motion and vibration-excitation tests driven by step or sinusoidal tendon inputs [2] [3], fast shape reconfiguration under external loading [4], vibration-suppressed trajectory tracking [5], and high-speed dynamic trajectory tracking based on accurate dynamic models [6]. In such settings, the strong coupling among inertia, damping, and actuation effects makes empirical or quasi-static models inadequate for accurate dynamic prediction and control [7]. Thus, developing dynamically consistent and computationally efficient models is crucial for advancing CDCRs toward high-performance dynamic operation [8]–[10].

Early studies based on geometric assumptions introduced the Piecewise Constant Curvature (PCC) empirical model for the kinematic modeling of CDCRs [11], [12]. Subsequent work extended PCC to dynamic modeling by treating segment-level generalized parameters as system states and incorporating equivalent inertia, damping, and actuation terms [3], [8], [9]. However, under significant distributed loads or geometric nonuniformities, PCC-based models lose accuracy in capturing curvature distribution and dynamic

response [12]. Although variable- and polynomial-curvature models improve precision [9], they increase computational complexity and the cost of parameter identification [10].

Beyond geometric and empirical approaches, data-driven and learning-based methods have also been explored for dynamic modeling and compensation, including iterative learning-based identification [13], Koopman operator embeddings [14], and deep Koopman frameworks for nonlinear dynamics approximation [15]. While capable of capturing complex loading and coupling effects, these methods are sensitive to data quality and feature representations and often require substantial computational and training resources [16]. Their generalizability, interpretability, and control suitability still depend on integration with physical priors [14], [15].

In contrast, physics-based dynamic formulations such as FEM [17] and rod theories [18] systematically capture coupled bending, torsion, and axial deformation, providing higher predictive accuracy under complex loading and geometric variations [19]. However, these formulations are strongly nonlinear and high-dimensional, making real-time simulation challenging [19], [20]. To improve computational efficiency, model reduction and parameterization strategies have been developed, including Model Order Reduction (MOR) [20] and strain-based parameterizations [21], [22], with recent efforts even enabling real-time differentiable modeling through analytical derivatives in the time domain [23].

While physics-based dynamic formulations and reduced-order models have recently achieved real-time performance [23], their body-frame potential-energy representations, Lie-group variational operations, and space–time strain discretizations often result in complex formulations that are difficult to implement and generalize, especially for users without a specialized background. Motivated by these limitations and inspired by [24], we streamline the physical modeling for cable-driven actuation and obtain a more compact and tractable dynamic formulation. To this end, we propose the Lightweight Actuation-Space Energy Modeling (LASEM) framework, which formulates actuation potential energy directly in actuation space and, together with the proposed Galerkin-based PDE solver, enables lightweight, accurate, and computationally efficient dynamic modeling. The key novelty and contributions are summarized as follows:

Key Novelty. We propose a novel actuation-space energy formulation for CDCRs that expresses external potential energy entirely in actuation space, enabling a compact and tractable dynamic representation through direct variational derivation.

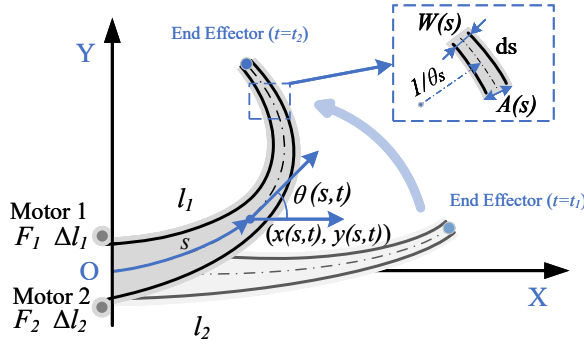


Fig. 1: A Cable-driven Continuum Robot

Contributions.

- **Single-PDE dynamic formulation.** A unified variational derivation producing a single governing PDE that requires only the Euler moment balance while implicitly satisfying the Newton force balance.
- **No contact-force computation.** The actuation-space formulation removes the need for explicit cable-backbone contact-force modeling, simplifying the dynamics and improving computational efficiency.
- **Displacement- and force-input compatibility.** Native support for both displacement-input and force-input actuation, a capability rarely achieved in existing dynamic formulations.
- **Broad applicability.** A unified modeling interface adaptable to diverse actuation and geometry layouts: arbitrary tendon routings, and nonuniform geometries.
- **Substantial computational speedup.** Using a Galerkin-based modal discretization yields analytical time-domain derivatives of the reduced state, which in turn enable LASEM to achieve an average 62.3% speedup over state-of-the-art real-time dynamic models.

II. LASEM DYNAMIC MODELING FRAMEWORK

This section details the LASEM dynamic modeling framework through a systematic derivation. The CDCR illustrated in Fig. 1 is parameterized as a geometrically nonlinear Euler-Bernoulli beam with spatially varying second moment of area $I(s)$, cross-sectional area $A(s)$, and cable spacing $W(s)$, with two inextensible cables symmetrically embedded along its sides. The motor-generated forces $F_1(t)$ and $F_2(t)$ act on the two cables as external inputs, producing the corresponding cable lengths $l_1(t)$ and $l_2(t)$ along the robot body, with displacements $\Delta l_1 = L - l_1$ and $\Delta l_2 = L - l_2$. The arc-length coordinate is $s \in [0, L]$, $\theta(s, t)$ denotes the bending angle, and $\theta_s(s, t)$ denotes the curvature. The backbone position in the global frame is $(x(s, t), y(s, t))$. Throughout this paper, $(\cdot)_t = \partial(\cdot)/\partial t$, $(\cdot)_{tt} = \partial^2(\cdot)/\partial t^2$, $(\cdot)_s = \partial(\cdot)/\partial s$, and $(\cdot)_{ss} = \partial^2(\cdot)/\partial s^2$.

A. Kinematics and Geometric Constraints

The backbone geometry of the studied CDCR is given by

$$x(s, t) = \int_0^s \cos \theta(\xi, t) d\xi, \quad y(s, t) = \int_0^s \sin \theta(\xi, t) d\xi. \quad (1)$$

Following the curvature-tendon displacement relation in [24], the differential cable actuation satisfies

$$\Delta l(t) = \Delta l_1 = -\Delta l_2 = \frac{1}{2} \int_0^L W(s) \theta_s(s, t) ds, \quad (2)$$

which serves as the boundary constraint for the dynamic model derived in the next subsection.

B. Derived Dynamic Models through Functional Variation

1) *Dynamic Modeling with Force Input:* The system Lagrangian is defined as

$$L_F[\theta] = T_{\text{rot}} + T_x + T_y - U_b - G - F_1 \Delta l_1 - F_2 \Delta l_2. \quad (3)$$

Substituting (2) into (3) yields the compact Lagrangian form

$$L_F[\theta] = T_{\text{rot}} + T_x + T_y - U_b - G - \frac{\Delta_F(t)}{2} \int_0^L \theta_s(s, t) W(s) ds. \quad (4)$$

where $\Delta_F(t) = F_1 - F_2$. The energy terms are given by

$$\begin{aligned} T_{\text{rot}} &= \frac{1}{2} \rho \int_0^L I(s) \theta_t^2 ds, \quad T_x = \frac{1}{2} \rho \int_0^L A(s) M_x(s, t)^2 ds, \\ T_y &= \frac{1}{2} \rho \int_0^L A(s) M_y(s, t)^2 ds, \quad U_b = \frac{1}{2} E \int_0^L I(s) \theta_s^2 ds, \\ G &= \int_0^L q_x(s) \left[s - \int_0^s \cos \theta(\sigma, t) d\sigma \right] ds - \int_0^L q_y(s) \int_0^s \sin \theta(\sigma, t) d\sigma ds, \end{aligned} \quad (5)$$

where

$$\begin{aligned} M_x(s, t) &= \int_0^s \theta_t(\sigma, t) \sin \theta(\sigma, t) d\sigma, \\ M_y(s, t) &= \int_0^s \theta_t(\sigma, t) \cos \theta(\sigma, t) d\sigma. \end{aligned}$$

Finally, the corresponding action functional is

$$S_F[\theta] = \int_{t_0}^{t_1} L_F[\theta(s, t)] dt. \quad (6)$$

According to Hamilton's principle, the physical motion renders $S_F[\theta]$ stationary, thereby ensuring the balance between kinetic and potential energies. To apply Hamilton's principle, we evaluate the variation of each energy term in the Lagrangian $L_F[\theta]$ defined in (3). The variation of the rotational kinetic energy is

$$\int_{t_0}^{t_1} \delta T_{\text{rot}} dt = \rho \int_{t_0}^{t_1} \int_0^L I(s) \theta_t \delta \theta_t ds dt,$$

which after integration by parts in time becomes

$$\int_{t_0}^{t_1} \delta T_{\text{rot}} dt = - \int_{t_0}^{t_1} \int_0^L \rho I(s) \theta_{tt} \delta \theta ds dt. \quad (7)$$

For the translational kinetic energy T_x , we write

$$\int_{t_0}^{t_1} \delta T_x dt = \rho \int_{t_0}^{t_1} \int_0^L A(s) M_x(s, t) \delta M_x(s, t) ds dt, \quad (8)$$

where

$$\delta M_x(s, t) = \int_0^s [\delta \theta_t(\sigma, t) \sin \theta + \theta_t(\sigma, t) \cos \theta \delta \theta] d\sigma.$$

By exchanging the order of integration in (8), we obtain the compact expression

$$\int_{t_0}^{t_1} \delta T_x dt = \int_{t_0}^{t_1} \int_0^L \rho \sin \theta(\sigma, t) \mathcal{J}_x(\sigma, t) \delta \theta(\sigma, t) d\sigma dt, \quad (9)$$

where

$$\mathcal{J}_x(\sigma, t) = \int_{\sigma}^L A(\xi) \int_0^{\xi} [\theta_{tt}(\eta, t) \sin \theta + \theta_t(\eta, t)^2 \cos \theta] d\eta d\xi.$$

Following a similar derivation to that of T_x , the final expression of the variation of T_y is obtained as

$$\int_{t_0}^{t_1} \delta T_y dt = - \int_{t_0}^{t_1} \int_0^L \rho \cos \theta(\sigma, t) \mathcal{J}_y(\sigma, t) \delta \theta(\sigma, t) d\sigma dt, \quad (10)$$

where

$$\mathcal{J}_y(\sigma, t) = \int_{\sigma}^L A(\xi) \int_0^{\xi} [\theta_{tt}(\eta, t) \cos \theta - \theta_t(\eta, t)^2 \sin \theta] d\eta d\xi.$$

The variations of the remaining potential terms are obtained as follows. The variation of the bending potential energy is

$$\delta U_b = E \int_0^L I(s) \theta_s(s, t) \delta \theta_s(s, t) ds.$$

Integrating by parts with respect to s gives

$$\begin{aligned} \delta U_b &= \mathcal{B}_1 - E \int_0^L [I(s) \theta_s(s, t)]_s \delta \theta(s, t) ds \\ &= \mathcal{B}_1 - \int_0^L E [I_s(s) \theta_s(s, t) + I(s) \theta_{ss}(s, t)] \delta \theta(s, t) ds, \end{aligned} \quad (11)$$

where

$$\mathcal{B}_1 = [E I(s) \theta_s(s, t) \delta \theta(s, t)]_{s=0}^{s=L}. \quad (12)$$

The variation of the external distributed loading term is

$$\delta G = \int_0^L [Q_x(s) \sin \theta(s, t) - Q_y(s) \cos \theta(s, t)] \delta \theta(s, t) ds. \quad (13)$$

where

$$Q_x(s) = \int_s^L q_x(\xi) d\xi, \quad Q_y(s) = \int_s^L q_y(\xi) d\xi.$$

Next, we evaluate the variation of the actuation term

$$\delta [-\Delta_F(t) \Delta l(t)] = -\frac{\Delta_F(t)}{2} \int_0^L W(s) \delta \theta_s(s, t) ds. \quad (14)$$

Integrating by parts with respect to s yields

$$\delta [-\Delta_F(t) \Delta l(t)] = \frac{\Delta_F(t)}{2} \int_0^L W_s(s) \delta \theta(s, t) ds - \mathcal{B}_2, \quad (15)$$

where

$$\mathcal{B}_2 = \left[\frac{\Delta_F(t)}{2} W(s) \delta \theta(s, t) \right]_{s=0}^{s=L}. \quad (16)$$

Collecting the results in Eqs. (7), (9), (10), (11), (13) together with (15), and noting that $\delta \theta$ is arbitrary, the stationarity condition $\delta S_F = 0$ leads to the governing dynamic equation

$$\rho I(s) \theta_{tt}(s, t) + \rho \mathcal{J}(s, t) = [E I(s) \theta_s(s, t)]_s + \frac{\Delta_F(t)}{2} W_s(s) + \mathcal{Q}(s, t). \quad (17)$$

The boundary condition follows from the combined boundary terms in Eqs. (12) and (16)

$$\mathcal{B}_1 - \mathcal{B}_2 = \left[[E I(s) \theta_s(s, t) + \frac{\Delta_F(t)}{2} W(s)] \delta \theta(s, t) \right]_0^L. \quad (18)$$

Since $\delta \theta$ is arbitrary at $s = L$, the natural moment boundary condition is

$$E I(L) \theta_s(L, t) + \frac{\Delta_F(t)}{2} W(L) = 0. \quad (19)$$

Integrating Eq. (17) with respect to s from 0 to L incorporates the above boundary condition into the dynamic formulation

$$\rho \int_0^L I(s) \theta_{tt}(s, t) ds + \rho \int_0^L \mathcal{J}(s, t) ds = -\frac{\Delta_F(t)}{2} W(0) + \int_0^L \mathcal{Q}(s, t) ds, \quad (20)$$

where

$$\begin{aligned} \mathcal{J}(s, t) &= \sin \theta(s, t) \mathcal{J}_x(s, t) + \cos \theta(s, t) \mathcal{J}_y(s, t), \\ \mathcal{J}_x(s, t) &= \int_s^L A(\xi) \int_0^{\xi} [\theta_{tt}(\eta, t) \sin \theta(\eta, t) + \theta_t(\eta, t)^2 \cos \theta(\eta, t)] d\eta d\xi, \\ \mathcal{J}_y(s, t) &= \int_s^L A(\xi) \int_0^{\xi} [\theta_{tt}(\eta, t) \cos \theta(\eta, t) - \theta_t(\eta, t)^2 \sin \theta(\eta, t)] d\eta d\xi, \\ \mathcal{Q}(s, t) &= Q_y(s) \cos \theta(s, t) - Q_x(s) \sin \theta(s, t). \end{aligned} \quad (21)$$

The initial and boundary conditions are

$$\theta(s, 0) = 0, \quad \theta_t(s, 0) = 0, \quad \theta(0, t) = 0. \quad (22)$$

2) *Dynamic Modeling with Displacement Inputs:* In most existing dynamic formulations for CDCRs, cable tension forces are used as the actuation inputs [1]. In practice, however, true force control is difficult because accurate tendon force sensing requires inline load cells [25], and estimating tension from motor current is unreliable due to gearbox friction [26], [27]. As a result, many controllers directly command cable displacements while assuming a monotonic displacement–tension relationship [28], [29], which does not constitute actual force control and limits the benefits of dynamic modeling. To address this gap, we introduce a displacement-input formulation that treats the cable displacement variation $\Delta l(t)$ as the actuation variable. The corresponding Lagrangian is

$$L_D[\theta] = T_{\text{rot}} + T_x + T_y - U_b - G, \quad (23)$$

where T_{rot} , T_x , T_y , U_b , and G are defined in the same manner as in Eq. (5), and $\Delta l(t)$ still satisfies the constraint (2). The action functional is

$$S_D[\theta(s, t)] = \int_{t_0}^{t_1} L_D[\theta(s, t)] dt. \quad (24)$$

Incorporating the constraint (2), the variational problem becomes

$$\begin{aligned} S_D[\theta(s, t)] &= \arg \min_{\theta(s, t)} \int_{t_0}^{t_1} L_D[\theta(s, t)] dt, \\ &\text{s.t. (2)}. \end{aligned} \quad (25)$$

To impose the constraint, we introduce a time-dependent Lagrange multiplier $\lambda(t)$ and define the augmented functional

$$\mathcal{H}_D(\theta, \lambda) = \int_{t_0}^{t_1} [L_D[\theta(s, t)] - \Psi(t)] dt, \quad (26)$$

where

$$\Psi(t) = \lambda(t) \left[\Delta l(t) - \frac{1}{2} \int_0^L \theta_s(s, t) W(s) ds \right].$$

Variation with respect to $\lambda(t)$ enforces the constraint, while variation with respect to $\theta(s, t)$ yields the dynamic equation.

Algorithm 1 Analytical Derivatives via Galerkin Method

- 1: **Inputs:** Actuation $\Gamma(t)$ (force or displacement), distributed load $\mathcal{Q}(s)$, initial states $\mathbf{c}_0, (\mathbf{c}_0)_t$.
 - 2: **Initialization:** Precompute \mathbf{M} and $\int_0^L \Phi(s) ds$.
 - 3: **for** $k = 1$ to N **do**
 - 4: **Update:** From $[\mathbf{c}_{k-1}, (\mathbf{c}_{k-1})_t]$ evaluate \mathbf{K} , \mathbf{h} , \mathbf{f}_Q , and $\mathbf{f}_1(t_k)$.
 - 5: **Solve:** $(\mathbf{c}_k)_{tt} = [\mathbf{M} + \rho \mathbf{K}(\mathbf{c}_{k-1})]^{-1} (\mathbf{f}_Q - \rho \mathbf{h} + \mathbf{f}_1)$.
 - 6: **Update:** Update the generalized coordinates \mathbf{c}_k and velocities $(\mathbf{c}_k)_t$; reconstruct the configuration $\theta(s, t_k)$ and end-effector position (x, y) .
 - 7: **end for**
-

Taking the variation with respect to $\lambda(t)$ gives

$$\delta \lambda \mathcal{H}_D = - \int_{t_0}^{t_1} \left[\Delta l(t) - \frac{1}{2} \int_0^L \theta_s(s, t) W(s) ds \right] \delta \lambda(t) dt. \quad (27)$$

implying (2) since $\delta \lambda(t)$ is arbitrary. The variation of the multiplier term is

$$\begin{aligned} \delta \Psi &= - \frac{1}{2} \int_{t_0}^{t_1} \lambda(t) \left[\int_0^L W(s) \delta \theta_s(s, t) ds \right] dt \\ &= - \int_{t_0}^{t_1} \mathcal{B}_3 dt + \frac{1}{2} \int_{t_0}^{t_1} \lambda(t) \left[\int_0^L W_s(s) \delta \theta(s, t) ds \right] dt, \end{aligned} \quad (28)$$

where the boundary term is

$$\mathcal{B}_3 = \left[\frac{\lambda(t)}{2} W(s) \delta \theta(s, t) \right]_0^L. \quad (29)$$

Collecting the variations in Eqs. (7), (9), (10), (11), (13), and (28), and enforcing $\delta S_D = 0$, we obtain

$$\rho I(s) \theta_{tt}(s, t) + \rho \mathcal{J}(s, t) = \left[EI(s) \theta_s(s, t) \right]_s - \frac{\lambda(t)}{2} W_s(s) + \mathcal{Q}(s, t), \quad (30)$$

The boundary contributions from Eqs. (12) and (29) give

$$\mathcal{B}_1 - \mathcal{B}_3 = \left[[EI(s) \theta_s(s, t) - \frac{\lambda(t)}{2} W(s)] \delta \theta(s, t) \right]_0^L.$$

Since $\delta \theta$ is arbitrary at $s = L$, the boundary condition is

$$EI(L) \theta_s(L, t) - \frac{\lambda(t)}{2} W(L) = 0. \quad (31)$$

Solving (31) yields

$$\lambda(t) = \frac{2EI(L) \theta_s(L, t)}{W(L)}. \quad (32)$$

Using the constraint (2) and integrating by parts,

$$\Delta l(t) = \frac{1}{2} W(L) \theta(L, t) - \frac{1}{2} \int_0^L W_s(s) \theta(s, t) ds. \quad (33)$$

Thus,

$$W(L) = \frac{2\Delta l(t) + \int_0^L W_s(s) \theta(s, t) ds}{\theta(L, t)}. \quad (34)$$

Substituting into (32) gives

$$\lambda(t) = \frac{2EI(L) \theta_s(L, t) \theta(L, t)}{2\Delta l(t) + \int_0^L W_s(s) \theta(s, t) ds}. \quad (35)$$

Finally, integrating Eq. (30) from $s = 0$ to $s = L$ yields

$$\rho \int_0^L I(s) \theta_{tt}(s, t) ds + \rho \int_0^L \mathcal{J}(s, t) ds = \frac{\lambda(t)}{2} W(0) + \int_0^L \mathcal{Q}(s, t) ds, \quad (36)$$

where $\mathcal{J}(s, t)$, $\mathcal{J}_x(s, t)$, $\mathcal{J}_y(s, t)$, and $\mathcal{Q}(s, t)$ follow the previous definitions (21).

III. DERIVATION OF ANALYTICAL DERIVATIVES VIA GALERKIN METHOD

To enable fast numerical computation, the partial differential equation under LASEM framework is projected onto a finite-dimensional coefficient space using the Galerkin method [30]. Let $\{\phi_j(s)\}_{j=0}^{m-1}$ denote the chosen basis functions, arranged as

$$\Phi(s) = [\phi_0(s), \dots, \phi_{m-1}(s)]^T, \quad \mathbf{c}_n = [c_0(t_n), \dots, c_{m-1}(t_n)]^T,$$

where $t_n = n\Delta t$ are discrete time nodes. Under this modal representation, the bending angle and its derivatives at step n are

$$\theta(s, n) = \Phi^T(s) \mathbf{c}_n, \quad \theta_t(s, n) = \Phi^T(s) (\mathbf{c}_n)_t, \quad \theta_{tt}(s, n) = \Phi^T(s) (\mathbf{c}_n)_{tt}. \quad (37)$$

Substituting (37) into the dynamic equation and enforcing the Galerkin orthogonality condition with respect to each basis $\phi_i(s)$ yields the discretized dynamics. At time step n , the system equation becomes

$$[\mathbf{M} + \rho \mathbf{K}(\mathbf{c}_{n-1})] (\mathbf{c}_n)_{tt} = \mathbf{f}_Q(\mathbf{c}_{n-1}) - \rho \mathbf{h}[\mathbf{c}_{n-1}, (\mathbf{c}_{n-1})_t] + \mathbf{f}_1(t_n), \quad (38)$$

where the system matrices and vectors are

$$\begin{aligned} \mathbf{M} &= \rho \int_0^L I(s) \Phi(s) \Phi^T(s) ds, \\ \mathbf{K}(\mathbf{c}_n) &= \int_0^L \left[\sin \theta(s, n) \Xi^{(\sin)}(s, n) + \cos \theta(s, n) \Xi^{(\cos)}(s, n) \right] ds, \\ \mathbf{f}_Q(\mathbf{c}_n) &= \int_0^L \Phi(s) [Q_y(s) \cos \theta(s, n) - Q_x(s) \sin \theta(s, n)] ds, \\ \mathbf{f}_1(t_n) &= \Gamma(t_n) W(0) \int_0^L \Phi(s) ds. \end{aligned}$$

The intermediate coupling terms are

$$\begin{aligned} \Xi^{(\sin)}(s, n) &= \left[\int_s^L A(\xi) \int_0^\xi \Phi(\varpi) \sin \theta(\varpi, n) d\varpi d\xi \right] \Phi^T(s), \\ \Xi^{(\cos)}(s, n) &= \left[\int_s^L A(\xi) \int_0^\xi \Phi(\varpi) \cos \theta(\varpi, n) d\varpi d\xi \right] \Phi^T(s). \end{aligned}$$

The Coriolis and centrifugal vector is

$$\begin{aligned} \mathbf{h}[\mathbf{c}_n, (\mathbf{c}_n)_t] &= \int_0^L \Phi(s) \left[\sin \theta(s, n) \int_s^L A(\xi) \int_0^\xi \theta_t^2(\varpi, n) \cos \theta(\varpi, n) d\varpi d\xi \right. \\ &\quad \left. - \cos \theta(s, n) \int_s^L A(\xi) \int_0^\xi \theta_t^2(\varpi, n) \sin \theta(\varpi, n) d\varpi d\xi \right] ds. \end{aligned}$$

It is noteworthy that the proposed actuation-space formulation naturally unifies both force-input and displacement-input models. The boundary actuation coefficient is

$$\Gamma(t_n) = \begin{cases} -\frac{1}{2} \Delta_F(t_n), & \text{Force-Input,} \\ +\frac{1}{2} \lambda(t_n), & \text{Displacement-Input.} \end{cases}$$

Based on this unified actuation treatment, the accelerated computational framework is implemented via an explicit temporal discretization strategy, summarized in Algorithm 1.

TABLE I: Simulation and Experimental Parameters

Parameter	Symbol	Value	Unit
Manipulator length	L	0.40	m
Cross-sectional diameter	D	0.004	m
Young's modulus	E	2×10^9	Pa
Cable spacing	W	0.11	m
Second moment of area	I	1.26×10^{-11}	m^4
Cross-sectional area	A	1.26×10^{-5}	m^2
Distributed gravity load	$q_y; q_x$	1.4794; 0	N/m
Viscous damping coefficient	c	16	N-m-s/rad

Note: Viscous damping in CDCR dynamics is commonly modeled as $c \dot{\theta}$ [20]. LASEM adopts this standard form by adding $c \dot{\theta}$ to (20) and (36), with the coefficient c identified from the dissipative behavior of the Cosserat-rod formulations to ensure consistent damping across formulations.

IV. NUMERICAL SIMULATION AND MODEL VALIDATION

To evaluate the accuracy and computational efficiency of the proposed LASEM framework, numerical simulations were conducted under diverse conditions. Within LASEM, two solution strategies were examined: a conventional spatial discretization (SD) scheme [31] and the proposed Galerkin formulation (38), which uses analytical time-domain derivatives. This internal comparison highlights the advantages of the Galerkin-based solver for the PDE derived in LASEM. The framework is further benchmarked against two established Cosserat-rod formulations, the Global Variable Strain (GVS) method [22] and its differentiable extension D-GVS [23], under identical inputs and boundary conditions. Across classic designs, nonuniform geometries, and arbitrary cable routings, the combination of LASEM and the Galerkin solver improved computational performance relative to the existing methods while preserving the physical consistency.

A. Case Studies and Settings

All simulations are conducted using the baseline physical and geometric parameters listed in Table I. To evaluate the generality of the proposed LASEM framework against Cosserat rod formulation, four representative cases are examined, each modifying one aspect of the structure, routing, or actuation while keeping all other parameters unchanged. The simulations were executed on a workstation equipped with an Intel Core i9-14900HX.

- **Case 1: Classic design.** All parameters follow Table I. The following actuation profiles are tested:
 - Linear input: $\Delta_F(t) = t$.
 - Sinusoidal input: $\Delta_F(t) = 1.5 - 0.3 \sin[2\pi(t - 1)]$.
 - High-speed step input: $\Delta_F(t) = 3u(t)$.

where $u(t)$ denotes a step function [32].

- **Case 2: Nonuniform geometries.** All baseline parameters are retained except the geometry, which follows

$$I(s) = \frac{\pi}{64} \left[D_0 + (D_1 - D_0) \frac{s}{L} \right]^4, \quad (39a)$$

$$A(s) = \frac{\pi}{4} \left[D_0 + (D_1 - D_0) \frac{s}{L} \right]^2, \quad (39b)$$

where $D_0 = 0.006, D_1 = 0.005$ are the base and tip diameters.

Tested actuation profiles:

- Linear input: $\Delta_F(t) = 2.75t$.

TABLE II: Computational Cost under Different Conditions

(a) Case 1: Classic Design

Model	Method	Linear Input	Sinusoidal Input	High-speed Step Input	Strain Order
LASEM	SD ^{1*}	2.662 s	2.278 s	1.557 s	NA ^{2*}
	Galerkin	0.213 s	0.107 s	0.088 s	6
Cosserat rod	GVS	NC ^{3*}	NC	NC	6
	D-GVS	0.523 s	0.425 s	0.242 s	6

(b) Case 2: Nonuniform geometries

Model	Method	Linear Input	Sinusoidal Input	High-speed Step Input	Strain Order
LASEM	SD	2.218 s	2.022 s	1.445 s	NA
	Galerkin	0.142 s	0.078 s	0.070 s	6
Cosserat rod	GVS	NC	NC	NC	6
	D-GVS	0.209 s	0.276 s	0.130 s	6

(c) Case 3: Arbitrary Cable Routing

Model	Method	Linear Input	Sinusoidal Input	High-speed Step Input	Strain Order
LASEM	SD	2.743 s	2.246 s	1.270 s	NA
	Galerkin	0.113 s	0.121 s	0.081 s	6
Cosserat rod	GVS	NC	NC	NC	6
	D-GVS	0.406 s	0.331 s	0.144 s	6

Note: 1* Spatial discretization (SD) is a standard technique for solving partial differential equations [31]. 2* NA denotes not applicable. Unlike the strain-order formulation, SD discretizes the system in space. 3* NC denotes non-convergence.

- Sinusoidal input: $\Delta_F(t) = 5 - 3 \sin[2\pi(t - 1)]$.
- High-speed ramp input: $\Delta_F(t) = 13.75u(t)$.

- **Case 3: Arbitrary cable routing.** The baseline model is used except that the cable spacing varies as

$$W(s) = 0.04 - 0.03 \left(\frac{s}{L} \right)^3. \quad (40)$$

Tested actuation profiles:

- Linear input: $\Delta_F(t) = 3.16t$.
- Sinusoidal input: $\Delta_F(t) = 5 - 3 \sin[2\pi(t - 1)]$.
- High-speed step input: $\Delta_F(t) = 8u(t)$.

- **Case 4: Displacement-input actuation.** Geometry follows Case 1; the actuation variable is tendon displacement $\Delta l(t)$. Tested input profiles:

- Linear inputs in classical designs and nonuniform geometries: $\Delta l(t) = 0.048(t - 1)$.

B. Numerical Results and Analysis

1) *Model Accuracy:* Numerical simulations were conducted using both the force-input model in Eq. (20) and the displacement-input model in Eq. (36). Representative results for all test cases are shown in Fig. 2. Across all input profiles in Cases 1–4, the deformation shapes predicted by LASEM (SD or Galerkin) generally agree with those obtained from the Cosserat-rod models (GVS or D-GVS), with only modest deviations. These differences arise from both modeling structure and numerical treatment: LASEM is governed by a single Euler–moment-balance PDE that implicitly enforces force balance, whereas Cosserat-rod formulations solve coupled force and moment equations, naturally

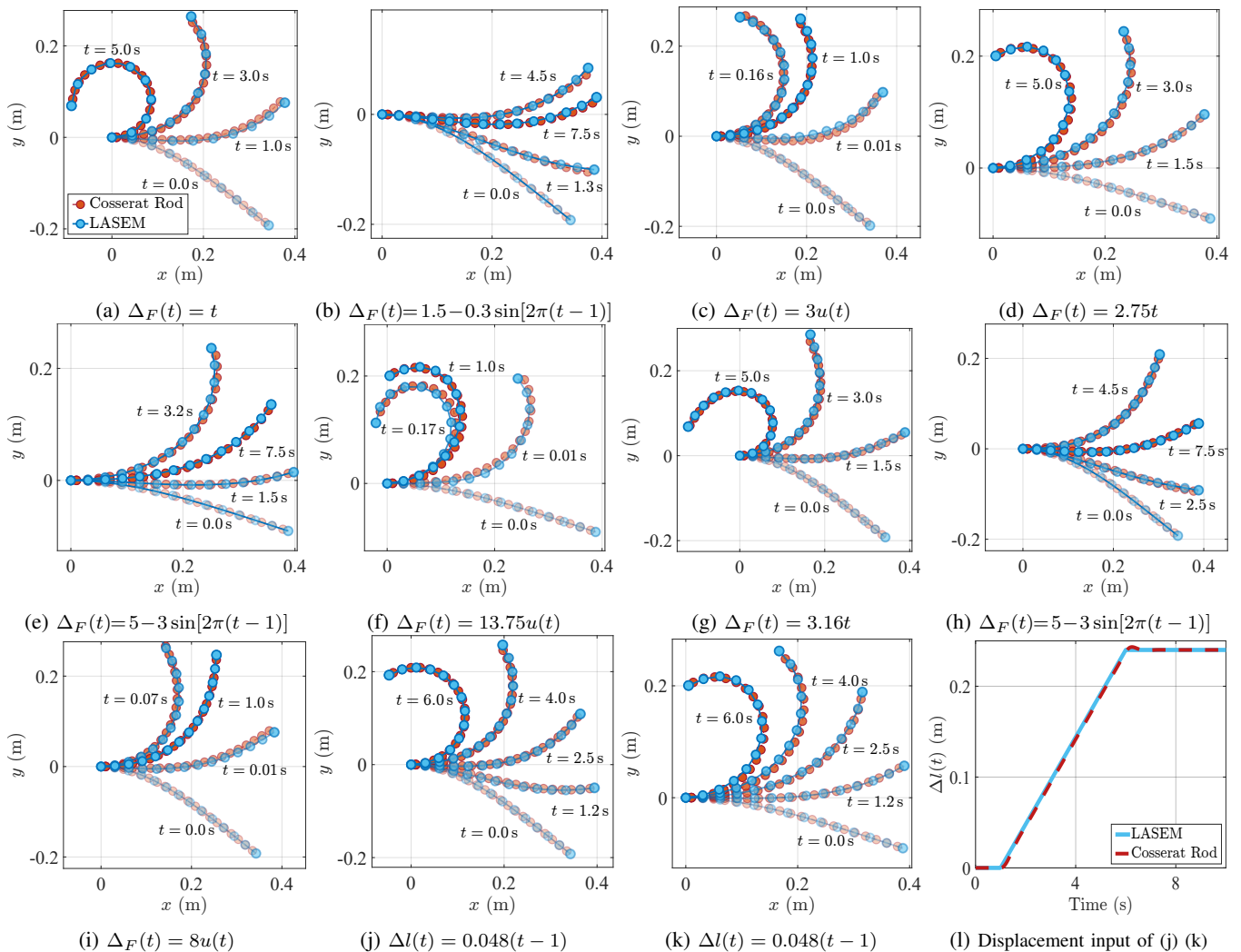


Fig. 2: Comparison of dynamic responses between LASEM and the Cosserat rod theory. Subfigures (2a)–(2c) correspond to classic designs (**Case 1**), (2d)–(2f) to nonuniform geometries (**Case 2**), (2g)–(2i) to arbitrary cable routings (**Case 3**), and (2j)–(2k) to displacement-input (**Case 4**), (2l) Displacement input for cases (2j) and (2k). $u(t)$ denotes a step function [32]. As with other dynamic models, the GVS formulation operates under force-input actuation [23]. A controller is therefore required to track the prescribed cable displacement and generate the corresponding force inputs for GVS models.

leading to different discretization characteristics. Moreover, the SD and Galerkin solvers of LASEM operate in scalar space, while Cosserat-rod models evolve Lie-group-valued variables whose orthogonality-preserving integration might introduce slight discrepancies in the resulting trajectories.

2) *Computational Expense*: Table II reports the computation times for all methods. Within the LASEM framework, the proposed Galerkin formulation achieves substantially faster computation than the traditional spatial discretization (SD) scheme [31], due to its analytical time-domain derivatives and reduced-dimensional representation. For broader benchmarking, the Galerkin-based LASEM model is also compared with the GVS and D-GVS formulations under identical boundary and input conditions. The relative efficiency is quantified by the speedup metric

$$\text{Speedup} = \frac{T_{\text{D-GVS}} - T_{\text{LASEM-Galerkin}}}{T_{\text{D-GVS}}}, \quad (41)$$

which measures the normalized reduction in runtime. Using this metric, the Galerkin-based LASEM implementation achieves an average **62.3% Speedup** across all test cases, outperforming D-GVS while maintaining high modeling accuracy.

V. EXPERIMENTAL VALIDATION

Physical experiments are conducted under displacement actuation, consistent with LASEM's displacement-input formulation in which the cable displacement $\Delta l(t)$ serves as the actuation input. This native compatibility (36) enables direct comparison between simulation and experiment.

A. Experimental Setup

As shown in Fig. 3, the CDCR is actuated by two DC motors prescribing differential cable displacements, and its posture is captured using a vision-based tracking system with planar AprilTag markers mounted along the backbone.

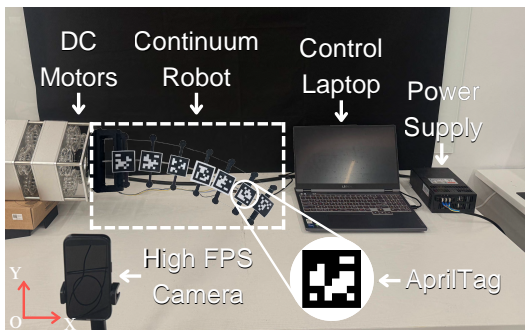


Fig. 3: Experimental Setup

Because the experiments involve rapid motions, a high-speed camera operating at 160 Hz is employed to ensure sufficient temporal resolution for accurate motion reconstruction. The geometric, material, and design parameters follow Table I; note that the parallel-axis cable routing is physically implemented through seven rigid disks that discretize the tendon paths along the backbone (Fig. 3).

B. Case Studies

To evaluate the dynamic performance of the proposed LASEM framework for dynamic modeling under different displacement actuation patterns, four representative cable-displacement inputs are tested. The input profiles and their mathematical expressions are summarized below.

- **Case A: Slow linear ramp:** $\Delta l(t) = 0.008t$.
- **Case B: Step input:** $\Delta l(t) = 0.14u(t)$.
- **Case C: Quick linear ramp followed by sinusoidal excitation:**

$$\Delta l(t) = \begin{cases} 0.04t, & 0 \leq t < 2, \\ 0.08 + 0.018 \sin[2\pi(t-2)], & t \geq 2. \end{cases}$$

- **Case D: Exponentially decaying sinusoidal input:**

$$\Delta l(t) = \begin{cases} 0.046 - 0.12 e^{-0.35t} \sin(2\pi t), & 0 \leq t < 4, \\ 0.046 & t \geq 4. \end{cases}$$

C. Experimental Results and Analysis

The comparisons between the measured configurations obtained from the high-speed camera and the simulated results are shown in Figs. (4a)–(4d), demonstrating close agreement in both deformation profiles and transient responses. Prediction accuracy is further assessed through backbone-shape trajectories in Figs. (4e)–(4h) and end-effector trajectories in Figs. (4i)–(4l). Across all input modes from **Case A** to **Case D**, the simulated responses produced by LASEM closely track the time-varying motions of the physical robot. The remaining discrepancies can be attributed to factors such as parameter-identification uncertainty and structural imperfections in the hardware (e.g., nonideal parallel cable routing). Overall, the results show that LASEM provides a reliable approximation of the robot’s dynamic behavior.

VI. CONCLUSIONS

This work introduced the Lightweight Actuation-Space Energy Modeling (LASEM) framework for dynamic modeling of CDCRs. By formulating actuation potential energy

directly in actuation space, LASEM yields a single Euler–moment–balance PDE that implicitly accounts for force balance and avoids explicit cable–backbone contact-force computation. The framework accommodates both force- and displacement-input actuation and applies naturally to nonuniform geometries and arbitrary cable routings. When combined with a Galerkin-based modal discretization that provides analytical time-domain derivatives, LASEM achieves an average **62.3%** computational speedup over existing real-time dynamic models. Numerical and experimental validations show that LASEM reproduces the manipulator’s deformation and dynamic responses with high fidelity and computational efficiency. Future work will extend LASEM to spatial CDCRs for full three-dimensional dynamic modeling.

REFERENCES

- [1] C. Della Santina, C. Duriez, and D. Rus, “Model-based control of soft robots: A survey of the state of the art and open challenges,” *IEEE Control Systems Magazine*, vol. 43, no. 3, pp. 30–65, 2023.
- [2] F. Renda, M. Giorelli, M. Calisti, M. Cianchetti, and C. Laschi, “Dynamic model of a multibending soft robot arm driven by cables,” *IEEE Transactions on Robotics*, vol. 30, no. 5, pp. 1109–1122, 2014.
- [3] M. Tummers, V. Lebastard, F. Boyer, J. Troccaz, B. Rosa, and M. T. Chikhaoui, “Cosserrat rod modeling of continuum robots from newtonian and lagrangian perspectives,” *IEEE Transactions on Robotics*, vol. 39, no. 3, pp. 2360–2378, 2023.
- [4] N. Li, F. Li, H. Yang, and H. Peng, “Real-time control of a soft manipulator based on reduced order extended position-based dynamics,” *Mechanism and Machine Theory*, vol. 202, p. 105774, 2024.
- [5] M. Pierallini, F. Stella, F. Angelini, B. Deutschmann, J. Hughes, A. Bicchi, M. Garabini, and C. Della Santina, “A provably stable iterative learning controller for continuum soft robots,” *IEEE Robotics and Automation Letters*, vol. 8, no. 10, pp. 6427–6434, 2023.
- [6] D. Caradonna, M. Pierallini, C. Della Santina, F. Angelini, and A. Bicchi, “Model and control of r-soft inverted pendulum,” *IEEE Robotics and Automation Letters*, vol. 9, no. 6, pp. 5102–5109, 2024.
- [7] T. George Thuruthel, Y. Ansari, E. Falotico, and C. Laschi, “Control strategies for soft robotic manipulators: A survey,” *Soft robotics*, vol. 5, no. 2, pp. 149–163, 2018.
- [8] C. Della Santina, C. Duriez, and D. Rus, “Model-based control of soft robots: A survey of the state of the art and open challenges,” *IEEE Control Systems Magazine*, vol. 43, no. 3, pp. 30–65, 2023.
- [9] C. Armanini, F. Boyer, A. T. Mathew, C. Duriez, and F. Renda, “Soft robots modeling: A structured overview,” *IEEE Transactions on Robotics*, vol. 39, no. 3, pp. 1728–1748, 2023.
- [10] J. Till, V. Aloï, and C. Rucker, “Real-time dynamics of soft and continuum robots based on cosserat rod models,” *The International Journal of Robotics Research*, vol. 38, no. 6, pp. 723–746, 2019.
- [11] G. S. Chirikjian, *Theory and applications of hyper-redundant robotic manipulators*. California Institute of Technology, 1992.
- [12] C. Della Santina and D. Rus, “Control oriented modeling of soft robots: The polynomial curvature case,” *IEEE Robotics and Automation Letters*, vol. 5, no. 2, pp. 290–298, 2019.
- [13] M. Pierallini, F. Stella, F. Angelini, B. Deutschmann, J. Hughes, A. Bicchi, M. Garabini, and C. Della Santina, “A provably stable iterative learning controller for continuum soft robots,” *IEEE Robotics and Automation Letters*, vol. 8, no. 10, pp. 6427–6434, 2023.
- [14] D. Bruder, X. Fu, R. B. Gillespie, C. D. Remy, and R. Vasudevan, “Koopman-based control of a soft continuum manipulator under variable loading conditions,” *IEEE robotics and automation letters*, vol. 6, no. 4, pp. 6852–6859, 2021.
- [15] N. Komeno, B. Michael, K. Kuchler, E. Anarossi, and T. Matsubara, “Deep koopman with control: Spectral analysis of soft robot dynamics,” in *2022 61st Annual Conference of the Society of Instrument and Control Engineers (SICE)*. IEEE, 2022, pp. 333–340.
- [16] Z. Chen, F. Renda, A. Le Gall, L. Mocellin, M. Bernabei, T. Dangel, G. Ciuti, M. Cianchetti, and C. Stefanini, “Data-driven methods applied to soft robot modeling and control: A review,” *IEEE Transactions on Automation Science and Engineering*, vol. 22, pp. 2241–2256, 2024.

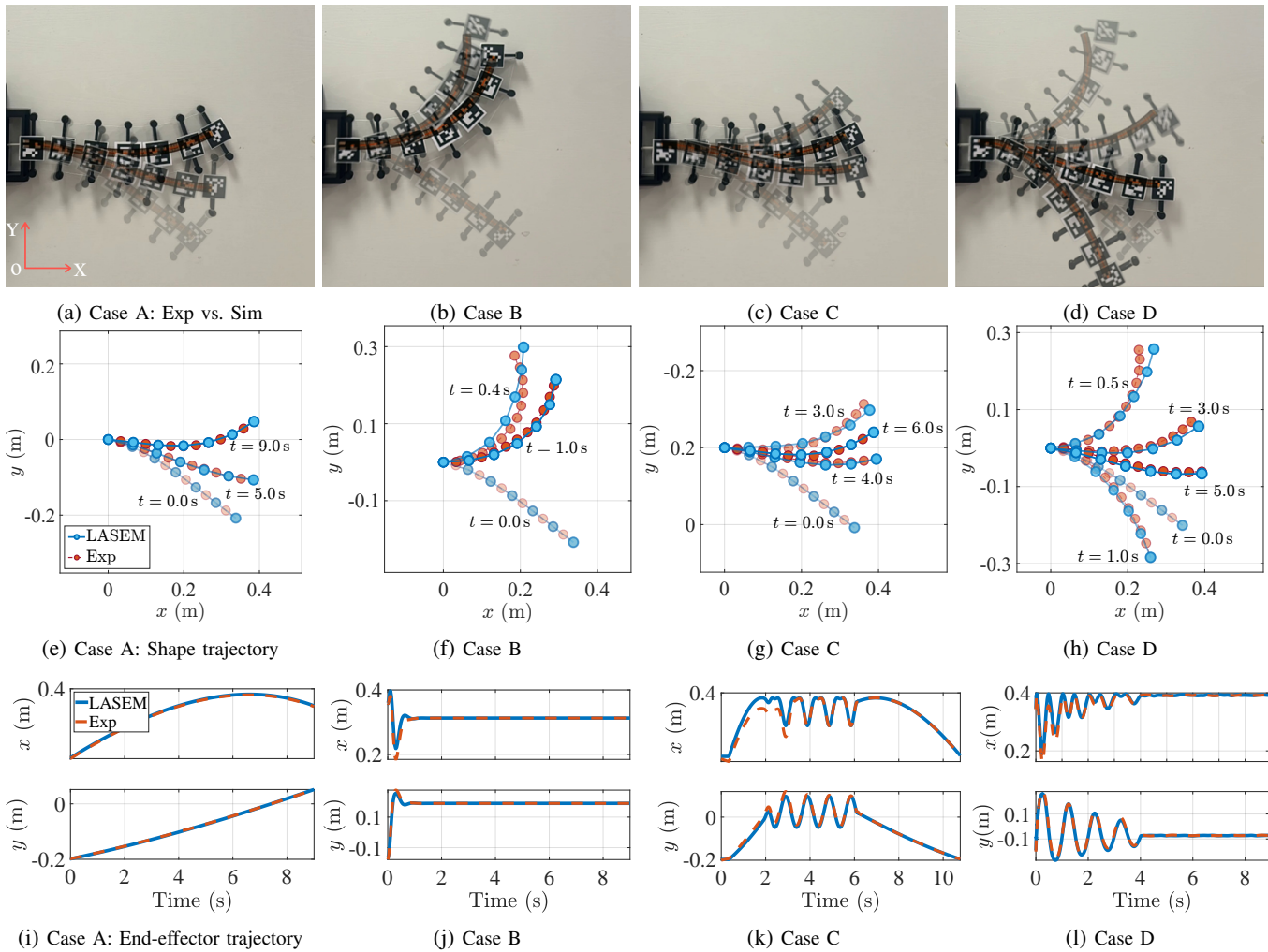


Fig. 4: Comparison between experimental measurements and simulation results across four test cases, including experiment vs. simulation comparisons (4a)-(4d), backbone-shape trajectory comparisons (4e)-(4h), and end-effector trajectory comparisons (4i)-(4l).

- [17] F. Faure, C. Duriez, H. Delingette, J. Allard, B. Gilles, S. Marchesseau, H. Talbot, H. Courtecuisse, G. Bousquet, I. Peterlik *et al.*, "Sofa: A multi-model framework for interactive physical simulation," in *Soft tissue biomechanical modeling for computer assisted surgery*. Springer, 2012, pp. 283–321.
- [18] F. Boyer, V. Lebastard, F. Candelier, and F. Renda, "Dynamics of continuum and soft robots: A strain parameterization based approach," *IEEE Transactions on Robotics*, vol. 37, no. 3, pp. 847–863, 2020.
- [19] C. Armanini, F. Boyer, A. T. Mathew, C. Duriez, and F. Renda, "Soft robots modeling: A structured overview," *IEEE Transactions on Robotics*, vol. 39, no. 3, pp. 1728–1748, 2023.
- [20] O. Goury and C. Duriez, "Fast, generic, and reliable control and simulation of soft robots using model order reduction," *IEEE Transactions on Robotics*, vol. 34, no. 6, pp. 1565–1576, 2018.
- [21] F. Renda, A. Mathew, and D. F. Talegon, "Dynamics and control of soft robots with implicit strain parameterization," *IEEE Robotics and Automation Letters*, vol. 9, no. 3, pp. 2782–2789, 2024.
- [22] A. T. Mathew, D. Feliu-Talegon, A. Y. Alkayaf, F. Boyer, and F. Renda, "Reduced order modeling of hybrid soft-rigid robots using global, local, and state-dependent strain parameterization," *The International Journal of Robotics Research*, vol. 44, no. 1, pp. 129–154, 2025.
- [23] A. T. Mathew, F. Boyer, V. Lebastard, and F. Renda, "Analytical derivatives of strain-based dynamic model for hybrid soft-rigid robots," *The International Journal of Robotics Research*, p. 02783649251346209.
- [24] K. Wu, Y. Wang, K. Henry, C. Stefanini, and G. Zheng, "Lightweight kinematic and static modeling of cable-driven continuum robots via actuation-space energy formulation," *arXiv preprint arXiv:2509.04119*, 2025.
- [25] A. Bajo and N. Simaan, "Hybrid motion/force control of multi-backbone continuum robots," *The International journal of robotics research*, vol. 35, no. 4, pp. 422–434, 2016.
- [26] A. G. Gonzalez-Rodriguez, E. Ottaviano, and P. Rea, "Evaluation of two tension sensors for cable-driven parallel manipulators," *Journal of Field Robotics*, vol. 42, no. 4, pp. 1191–1208, 2025.
- [27] J. Piao, E.-S. Kim, H. Choi, C.-B. Moon, E. Choi, J.-O. Park, and C.-S. Kim, "Indirect force control of a cable-driven parallel robot: Tension estimation using artificial neural network trained by force sensor measurements," *Sensors*, vol. 19, no. 11, p. 2520, 2019.
- [28] K. Wu and G. Zheng, "Fem-based nonlinear controller for a soft trunk robot," *IEEE Robotics and Automation Letters*, vol. 7, no. 2, pp. 5735–5740, 2022.
- [29] S. Li, A. Kruszewski, T.-M. Guerra, and A.-T. Nguyen, "Equivalent-input-disturbance-based dynamic tracking control for soft robots via reduced-order finite-element models," *IEEE/ASME Transactions on Mechatronics*, vol. 27, no. 5, pp. 4078–4089, 2022.
- [30] S. H. Sadati, S. E. Naghibi, I. D. Walker, K. Althoefer, and T. Nanayakkara, "Control space reduction and real-time accurate modeling of continuum manipulators using ritz and ritz-galerkin methods," *IEEE Robotics and Automation Letters*, vol. 3, no. 1, pp. 328–335, 2017.
- [31] R. J. LeVeque, *Finite difference methods for ordinary and partial differential equations: steady-state and time-dependent problems*. SIAM, 2007.
- [32] H. P. Hsu, *Signals and systems*. New York, 2011.